Journal of Materials Chemistry A

Accepted Manuscript

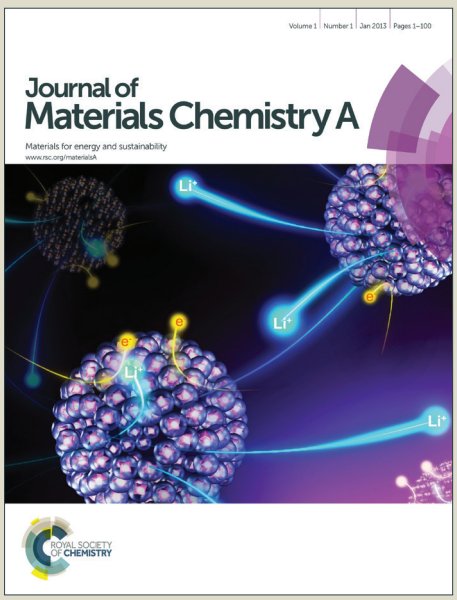

ROYAL SOCIETY OF CHEMISTRY

www.rsc.org/materialsA

Nameof Journal

Cite this: DOI: 10.1039/c0xx00000x

www.rsc.org/xxxxxx

ARTICLE TYPE

L-histidine-assisted template-free hydrothermal synthesis of α-Fe_2O_3 porous multi-shelled hollow spheres with enhanced lithium storage properties

Zhen-guo Wu,[a,b] Yan-jun Zhong,[a,b] Jun-tao Li,[b*] Xiao-dong Guo,[a*] Ling Huang,[b] Ben-he Zhong,[a] and Shi-gang Sun[b]

Received (in XXX, XXX) Xth XXXXXXXXX 20XX, Accepted Xth XXXXXXXXX 20XX
DOI: 10.1039/b000000x

Unique α-Fe_2O_3 porous multi-shelled hollow spheres (α-Fe_2O_3 PMSHSs) have been prepared by a simple template-free hydrothermal method followed by annealing in air. For the first time, L-histidine was used as morphology controlling agent in the synthesis process. The α-Fe_2O_3 PMSHSs had a relative high surface area of 14.2 m^2 g^{-1} and a pore volume of 0.07 cm^3 g^{-1}. When used as an anode material for lithium ion batteries, the α-Fe_2O_3 PMSHSs exhibited high specific capacity, good cycling stability, and excellent rate performance. A stable and reversible capacity of 869.9 mAh g^{-1} could be maintained at a charge-discharge current density of 400 mA g^{-1} after 300 cycles. Superior rate capability had also been demonstrated by testing the material at different current densities. The α-Fe_2O_3 PMSHSs could deliver a capacity as high as 833.3 mAh g^{-1} at 800 mA g^{-1}, and a capacity of 498.1 mAh g^{-1} at 6000 mA g^{-1}. The superior electrochemical performance of the α-Fe_2O_3 PMSHSs is attributed to the hierarchical porosity, special micro/nano structure, shorten electron and lithium ions diffusion pathways, and easy penetration of electrolyte.

1. Introduction:

Multi-shelled hollow spheres (MSHSs) materials, with high surface area, high pore volume, high void space and shell permeability, have attracted tremendous attention in lithium ion batteries (LIBs).[1] Since the high pore volume and void space allow for better accommodation of dramatic volume changes during repeated lithiation/delithiation process, resulting in better structure stability and cycling performance. The permeable and porous thin shells shorten greatly the distance for the diffusion of electron and Li^+, enhancing the rate capability. The porous hollow structure with a high surface area also has more location for Li ion storage, which helps to improve the capacity.[2-3] Normally, the procedure for the preparation of MSHSs involves the shell-by-shell deposition of desired materials onto sacrificial templates followed by selective template removal. Monodispersed polymers,[4] silica,[5] carbon,[6-7] and micelles[8-9] have been widely used as the sacrificial template. It suffers, however, some disadvantages with template routes, e.g., the difficulty in template fabrication, the possibility of product deconstruction during the template removal process, the shortage of templates for generating hollow structures with complex interiors, and multistep and costly operations. Therefore, to develop a simple and low-cost method for the fabrication of MSHSs materials becomes a significant subject in LIBs' studies.

According to the previous work of Tarascon et al., several transition metal oxides (TMOs), including Co_3O_4, Fe_2O_3, NiO, and CuO, etc., own their extremely high theoretical specific capacity via a conversion reaction,[10-12] which are promising alternative anode materials of graphite employed in commercial LIBs. Among the TMOs, the Fe_2O_3 has been extensively studied because of its high specific capacity (1007 mAh g^{-1} assuming 6 Li per formula unit), natural abundance, low-cost and non-toxicity.[13-17] Despite these advantages, the large volume changes during lithiation/delithiation process, which results in electrode pulverization and capacity fading, severely encumbered its practical application.[18] Therefore, some different strategies have been proposed to mitigate the above mentioned problem. One commonly used approach is to introduce a flexible and stable overlayer, such as amorphous carbon, as a physical scaffold to effectively counteract the pulverization.[19-24] The carbon component could also increase the electrical conductivity of nanocomposite. Another effective protocol is to design and create nanostructured Fe_2O_3 that can better sustain the volume variation, such as hollow and porous structures materials. It is also believed that these nanostructures with large exposed surface and short diffusion length could interact more efficiently with Li^+ ions, including nanowires,[25] nanoflakes,[16] nanotubes,[26] hollowspheres,[27] microcubes,[28] microboxes,[29] spindles,[30] nanorods,[17, 31-32] and so forth.

Recently, Hu and his coworkers synthesized multi-shelled α-Fe_2O_3 hollow spheres with two shells by a solvothermal method using carbon spheres as the hard template. But, they only focused on the enhanced visible-light photocatalytic activity without the potential application in electrochemical energy storage.[33] Yu and his co-workers obtained the α-Fe_2O_3 MSHSs with four shells by a spray drying method.[34] Although the α-Fe_2O_3 MSHSs exhibited high capacity and outstanding rate capability that demonstrates a promising application in LIBs, only a cycling performance of 50 cycles was conducted. Kang and his co-workers also have prepared Fe_2O_3 yolk-shell particles with two, or four shells by the spray drying method.[35] The Fe_2O_3 yolk-shell particles exhibited superior lithium storage properties. Their report reveals that Fe_2O_3 yolk-shell particles with more shells exhibit a better rate capability but relatively worse cycling performance. For the Fe_2O_3 yolk-shell particles with four shells, a high capacity of 1000 mAh g^{-1} only could be maintained at the first 30 cycles and a low capacity of ~300 mAh g^{-1} was measured after 80 cycles. Therefore, the synthesis of Fe_2O_3 anode materials possessing both long cycling performance and high rate capability still remain a great challenge. It is also important to find a simple and template-free method for the synthesis of materials with MSHSs structure.

Hydrothermal is an effective method for the synthesis of nanocomposite. The nanostructures could be controlled simply by choosing the proper reaction temperature, reaction time and solvents without employing templates.[36] Hydrothermal synthesis has been widely used in the synthesis of Fe_2O_3 materials with different nanoarchitectures, such as microspheres,[37] hollow spheres,[38] hollow urchin-like microstructures,[39] etc. In this study, we report a method for the synthesis of α-Fe_2O_3 porous multi-shelled hollow spheres (α-Fe_2O_3 PMSHSs) through a template-free hydrothermal route, in which L-histidine acted as a morphology-controlling agent. When used as anode electrode for LIBs, the as-prepared α-Fe_2O_3 porous MSHSs exhibit high specific capacity, superior rate capability and stable cycling performance.

2. Experimental

2.1 Preparation of α-Fe_2O_3 porous multi-shelled hollow spheres

The α-Fe_2O_3 PMSHSs were prepared through a hydrothermal methode followed by annealing in air. All reagents are analytically pure and used directly without further purification. In a typical experiment, 4 g L-histidine and 2 g $Fe(NO_3)_3{\cdot}9H_2O$ were dissolved in 30 ml deionized water. Then, the solution was homogenized by vigorous stirring. The resultant mixture was transferred to a 50 ml Teflon-lined autoclave and maintained at 180 °C for 12 h. After the reaction completed, the autoclave cooled to room temperature naturally. The precursors were obtained by centrifuging and sequentially washing with water and ethanol for several times and then dried in a vacuum oven at 80 °C for 12 h. Finally, the α-Fe_2O_3 PMSHSs were subjected to annealing at 600 °C for 2 h in air. To investigate the effect of L-histidine on morphology control in the synthesis of the α-Fe_2O_3 PMSHSs, several experiments involved different mass ratios (0.5:1, 1:1) of L-histidine to iron nitrate, $FeCl_3{\cdot}6H_2O$ instead of $Fe(NO_3)_3{\cdot}9H_2O$, L-arginine instead of L-histidine were performed to prepare Fe_2O_3 samples with the other fixed experiment conditions.

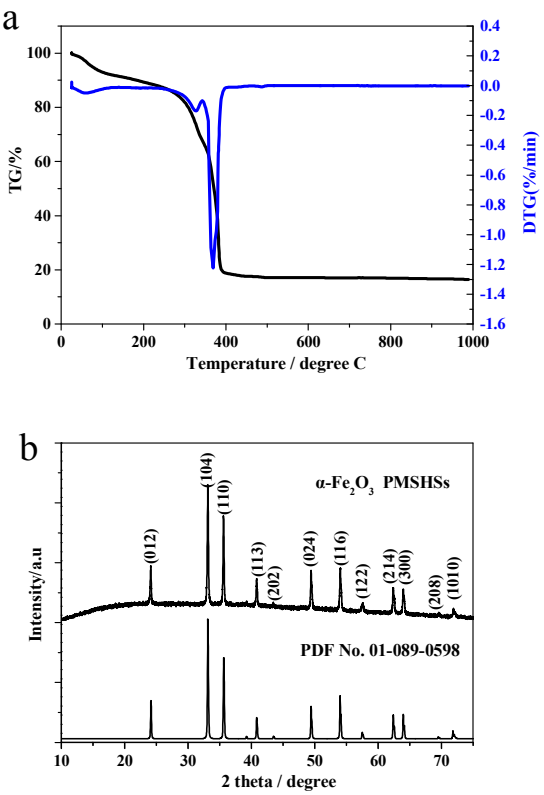

Fig.1 (a) TG and DTG curves of α-Fe_2O_3 PMSHSs precursor; (b) typical XRD pattern of α-Fe_2O_3 PMSHSs.

2.2 Characterization and electrochemical measurements

Thermogravimetric analysis was conducted on a simultaneous thermal analysis apparatus (SDT Q600, TA instrument) to determine the sintering temperature. The morphologies and structures of the as-prepared samples were characterized by field emission scanning electron microscopy (HITACHI S-4800), transmission electron microscopy (JEM 2100) and powder X-ray diffraction (XRD, Philips X'pert Pro Super X-ray diffract meter, Cu Kα radiation) measurements. The specific surface areas of the as-prepared samples were measured by the Brunauer-Emmett-Teller (BET) method using nitrogen adsorption and desorption isotherms on a Micrometics Tristar 3000 system. The electrodes were prepared by spreading a mixture of 75 wt% Fe_2O_3 active material, 15 wt% acetylene black and 10 wt% LA 132 onto a copper foil current collector. The as-prepared electrodes were dried at 80 °C in vacuum oven for 12 h. Electrochemical properties of the electrodes were measured by assembling them into coin cells (type CR2025) in an argon-filled glove box with water and oxygen contents less than 0.5 ppm. Lithium foil was used as counter electrode and polypropylene (PP) film (Celgard 2400) as the separator. The electrolyte was made from $LiPF_6$ (1 M) and a mixture of ethylene carbonate (EC)/dimethyl carbonate (DMC)/diethyl carbonate (DEC) in a volume ratio of 1:1:1 with 2 wt% vinylene carbonate (VC) as additive (purchased from Tinci Materials Technology Co., Ltd., Guangzhou, China). The cells were galvanostatically charged and discharged on a battery test system (LAND-2001A, Land Electronic Co., Ltd., Wuhan, China)

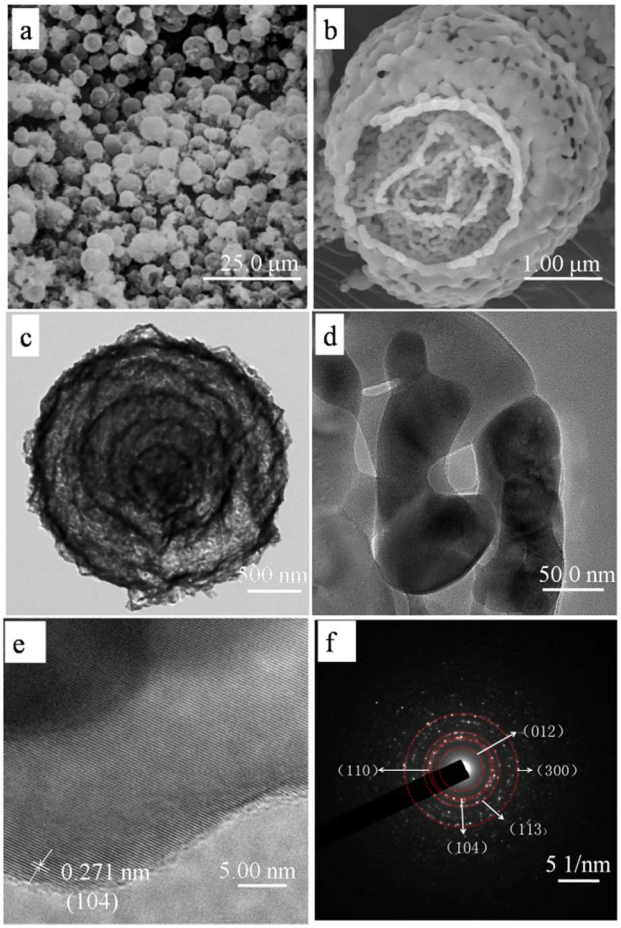

Fig.2 SEM images of α-Fe_2O_3 PMSHSs: (a) low magnification SEM image; (b) high magnification SEM images; TEM images (c, d), HRTEM image (e) and SAED pattern (f) of α-Fe_2O_3 PMSHSs.

with a cut-off voltage range of 0.01-3.00 V. Cyclic voltammetry (CV) was carried out on CHI 660D electrochemical workstation (CH Instruments Co., Ltd., Shanghai, China) using coin cell at a scan rate of 0.2 mV s^{-1} from 0.01 V to 3.00 V. The electrochemical tests were conducted at 30 °C. All potentials presented in this study were quoted versus the Li/Li^+ scale.

3. Results and discussion

3.1 Morphology and structure of α-Fe_2O_3 porous multi-shelled hollow spheres

Fig.1a shows TG/DTG curves of the precursor at a heating rate of 10 °C min^{-1} from ambient temperature to 1000 °C in air. The thermal decomposition of the precursor occurs at about 387 °C. Considering the reaction kinetics, and in order to guarantee a complete decomposition of the precursor in a relative short time, the calcination process was set at 600 °C for 2 h. The structure and chemical composition of the as-prepared sample was confirmed by XRD analysis at a scanning rate of 0.02 ° s^{-1} with 2 theta range of 10 - 75 °. Fig.1b illustrates the XRD pattern of the α-Fe_2O_3 PMSHSs after annealing the precursor at 600 °C for 2 h in air. All the diffraction peaks can be well indexed to the standard spectrum of α-Fe_2O_3 (PDF No.01-089-0598), with a space group of R-3c.

The morphologies and structures of the Fe_2O_3 samples were examined by scanning electron microscopy (SEM). Fig.2a and 2b

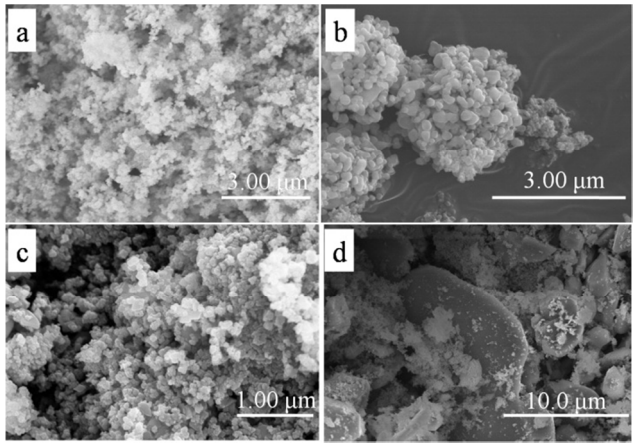

Fig.3 SEM images of α-Fe_2O_3 samples synthesized with different mass ratios of iron nitrate to L-histidine: (a) 0.5:1, (b) 1:1. (c) SEM image of α-Fe_2O_3 synthesized with L-arginine (2g $Fe(NO_3)_3$•$9H_2O$, 4g L-arginine), (d) SEM image of α-Fe_2O_3 synthesized with $FeCl_3$·$6H_2O$ (2 g $FeCl_3$·$6H_2O$, 4 g L-histidine).

illustrate SEM images of the α-Fe_2O_3 PMSHSs with an average diameter of ~3 μm. It can be observed that the α-Fe_2O_3 PMSHSs are assembled by about four porous shells, and the primary nanorods that formed the single shell have a diameter of ~50 nm and a length about 250 nm. To further examine the architecture of the α-Fe_2O_3 PMSHSs, the samples were investigated by TEM technique. TEM images shown in Fig.2c illustrate that the products have a multi-shelled hollow structure. The magnified region (Fig.2d) of a single microsphere indicates porous structure in the single shell, which is in good agreement with the SEM observations. Fig.2e is a typical high resolution TEM (HRTEM) image, in which the (104) lattice fringes of α-Fe_2O_3 can be clearly identified. The SAED pattern (Fig.2f) demonstrates a series of concentric rings indicating a polycrystalline structure. And the concentric rings can be assigned to the (012), (104), (110), (113) and (300) diffractions of α-Fe_2O_3, respectively. It should be noted that the L-histidine plays a crucial role in morphology controlled growth of α-Fe_2O_3 PMSHSs. The SEM images of α-Fe_2O_3 samples synthesized with different reagent mass ratios of iron nitrate to L-histidine are shown in Fig.3. When the ratio was set to 0.5:1 (Fig.3a), only nanoparticles materials are obtained. The results indicate that irregular aggregates of particles appear with a ratio of 1:1 (Fig.3b). Additionally, when L-arginine was used to synthesize α-Fe_2O_3 sample, the obtained product was also irregular aggregates of nanoparticles (Fig.3c). And when $FeCl_3$·$6H_2O$ was used to replace $Fe(NO_3)_3$·$9H_2O$, only irregular microparticles can be synthesized (Fig.3d). In conclusion, both L-histidine and NO_3^- ions play crucial roles in the synthesis of the α-Fe_2O_3 PMSHSs.

A hypothesis for the formation mechanism of the α-Fe_2O_3 PMSHSs is proposed as follows: During the synthesis process, part of insoluble L-histidine may act as crystal nucleus during the growth of the α-Fe_2O_3 PMSHSs precursor. Our experiment confirms that this special structure cannot be synthesized, when L-histidine was totally dissolved (Fig.S1). The dissolved L-histidine has strong coordination with Fe^{3+} ions, which results in the Fe(L-histidine)$^{3+}$ complex.[40] Meanwhile, L-histidine contains two amino groups and one carboxylic acid group. Its protein kinase A

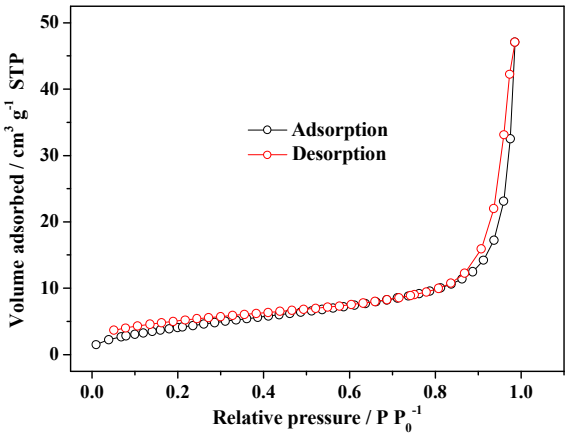

Fig.4 The gas (N_2) adsorption-desorption isotherm loop of α-Fe_2O_3 PMSHSs.

(pKa) is high enough and tends to bind with protons, which lead to the increase of OH^- concentration during the hydrothermal process.[37] And L-histidine with protons can form nonlinear molecular with NO_3^- ions.[41] Under a relative high temperature, Fe^{3+} ions was released from the complex to form amorphous $Fe(OH)_3$ by the reaction with OH^-(Fig.S2a).[42] Then $Fe(OH)_3$ nanoparticles, accompanying with L-histidine-H^+-NO_3^- nonlinear molecular, gathered on the crystal nucleus, to generate $Fe(OH)_3$-L-histidine-H^+-NO_3^-complex.[41, 43] The new complex changes to sphere-shape aggregation with a low surface energy after the hydrothermal treatment (Fig.S2b and 2c). Finally, the decomposition of amorphous $Fe(OH)_3$-L-histidine-H^+-NO_3^- complex during the calcinations process leads to the formation of the crystalline metal oxide phase, which bring size shrinkage effect and the phase separation to form the porous multi-shelled hollow spheres structure in the final product.[33]

BET measurement (Fig.4) indicates that the unique porous multi-shelled hollow structure gives rise to a surface area of 14.2 m^2 g^{-1} and a pore volume of 0.07 cm^3 g^{-1}.

3.2 Electrochemical performances of α-Fe_2O_3 PMSHSs

The electrochemical properties of the α-Fe_2O_3 PMSHSs anode were further investigated. The CV curves of the α-Fe_2O_3 PMSHSs are shown in Fig.5a. Two cathodic current peaks at 0.89 V and 0.68 V can be clearly observed in the first cycle. The high intensity peak initially at 0.68 V shifts to higher potential (0.78 V), and the peak at 0.89 V disappears in the subsequent cycling process. This can be interpreted by two factors: (1) the lithium insertion into the crystal structure of Fe_2O_3, the reversible conversion reaction of Fe_2O_3 with metallic lithium to form Li_2O and metal (Fe^0), and (2) the inevitable formation of solid electrolyte interphase (SEI) and irreversible reactions between lithium ions and electrode material.[44-46] In the anodic process, a broad peak appears at about 1.75 V, corresponding to the reversible conversion of metallic Fe to iron oxides.[47]

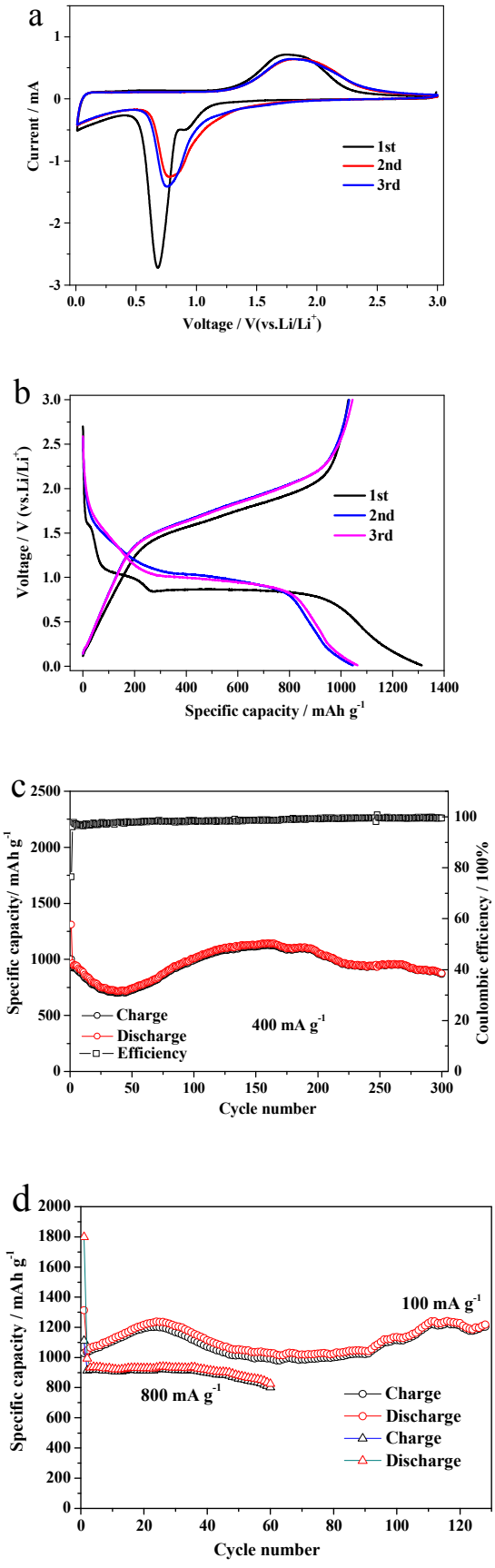

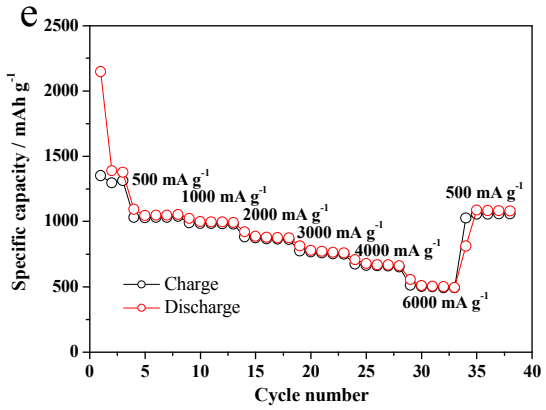

Fig.5 (a) The first three cyclic voltammethy (CV) curves of α-Fe_2O_3 PMSHSs at a scan rate of 0.2 mV s^{-1} in the voltage range of 0.01-3.00 V; (b) charge-discharge profilesα-Fe_2O_3 PMSHSs at 100 mA g^{-1}; (c) cycle performances of α-Fe_2O_3 PMSHSs at 400 mA g^{-1}; (d) cycle performances of α-Fe_2O_3 PMSHSs at 100 mA g^{-1} and 800 mA g^{-1}; (e) rate performances of α-Fe_2O_3 PMSHSs.

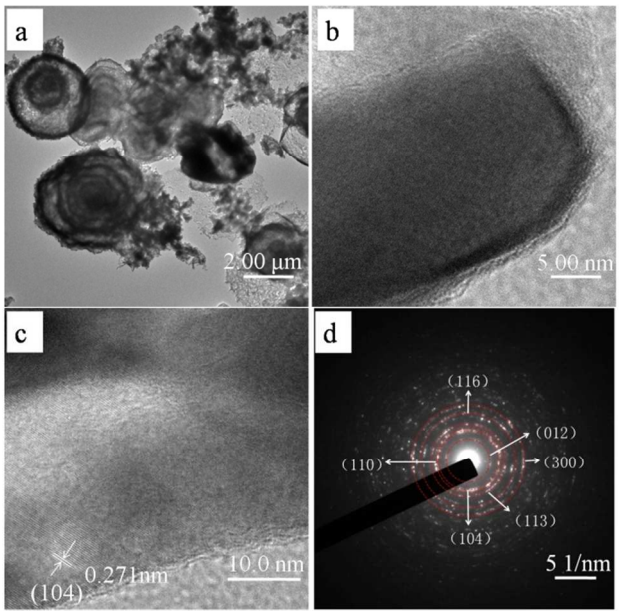

Fig.6 TEM images of α-Fe_2O_3 PMSHSs after 300 cycles: (a) low magnification TEM image; (b) high magnification TEM image; (c, d) HRTEM image and SAED pattern of α-Fe_2O_3 PMSHSs.

In the subsequent cycles, the anodic peak also positive shifts slightly to 1.8 V. The first three charge/discharge curves of the α-Fe_2O_3 PMSHSs obtained at a current density of 100 mA g^{-1} were presented in Fig.5b. The plateaus appeared in the charge/discharge curves are well consisted with the results of CVs. In the first cycle, the discharge and charge capacities were 1312.8 mAh g^{-1} and 1028.9 mAh g^{-1}, respectively, with an initial coulombic efficiency of 78.4%. The initial capacity loss may be mainly attributed to some irreversible processes such as electrolyte decomposition and formation of SEI layer, which also was observed in other transitional metal oxides.[48] The cycling performance of the α-Fe_2O_3 PMSHSs at 400 or 800 mA g^{-1} was obtained after the activating of half cells at 100 mA g^{-1} for one cycle. The cycling performance of the α-Fe_2O_3 PMSHSs at a current density of 400 mA g^{-1} was shown in Fig.5c. And after 300 charge/discharge cycles, the α-Fe_2O_3 PMSHSs could still maintain a high reversible charge capacity of 869.9 mAh g^{-1}, demonstrating an excellent cycleability. Fig.5d depicts the cycling performance of the α-Fe_2O_3 PMSHSs at 100 and 800 mA g^{-1}. After 128 charge/discharge cycles at 100 mA g^{-1}, a reversible charge capacity of 1202.8 mAh g^{-1} is obtained. And a capacity of 801.5 mAh g^{-1} can be obtained after 60 charge/discharge cycles at a high current density of 800 mA g^{-1}.

It is worthwhile to mention the capacity fluctuation phenomenon of the α-Fe_2O_3 PMSHSs during long-term cycling, which has been widely referred in the transition metal oxide electrodes.[13, 49-50] The reason could be partly ascribed to the reversible growth of a polymeric gel-like film on the surface of the progressively pulverized particles resulting from electrochemical grinding effect.[49] The difference of electrochemical performance at different current density could be related to the unique porous micro/nano structure, which is consistent with Yu's work.[49, 51] The rate performance of the α-Fe_2O_3 PMSHSs is illustrated further in Fig.5e. The cells are first activated at a current density of 100 mA g^{-1} for one cycle, and then the current density is successively increased to 500 mA g^{-1}, 1000 mA g^{-1}, 2000 mA g^{-1}, 3000 mA g^{-1} 4000 mA g^{-1} and 6000 mA g^{-1}. The corresponding average capacities are 1042.3, 993.2, 873.6, 770.4, 661.1 and 498.1 mAh g^{-1}, respectively. When the current density is decreased back to 500 mA g^{-1}, an average capacity of 1064.1 mAh g^{-1} can be recovered.

The morphology of the electrode after 300 charge/discharge cycles at a current density of 400 mA g^{-1} was presented to illustrate the stability. As shown in Fig.6a, some of the PMSHSs structure still is preserved after such a long time cycling process, indicating high structure stability. A thin SEI layer can be distinguished from the high magnification TEM image (Fig.6b). The results of SAED pattern and HRTEM image are consistent with Fig.2e and 2f. And the concentric rings can be assigned to the (012), (104), (110), (113), (116) and (300) diffractions of α-Fe_2O_3, respectively. Moreover, due to collapse of some α-Fe_2O_3 PMSHSs, the contacted interface between the active material and electrolyte increases. As a result, the fluctuation phenomenon of capacity has been observed in Fig.5c and 5d. It would cause loss of electrochemical contact and corresponding capacity fade with more and more α-Fe_2O_3 PMSHSs collapse. Therefore it is still a challenge to further enhance the structure stability of the electrode. The electrochemical performances of the α-Fe_2O_3 PMSHSs are also superior or at least comparable to those of the state-of-the-art Fe_2O_3 based anode materials reported recently, such as nanorods,[52] hollow spheres,[53-54] Fe_2O_3 carbon nanotubes,[55] Fe_2O_3-reduced grapheme oxide,[56] Fe_2O_3/GNS,[57] α-Fe_2O_3 MSHSs,[34-35] and Fe_2O_3 clusters.[58] The enhanced cycleability and rate capability of the α-Fe_2O_3 PMSHSs could be ascribed to their unique structure. First, the porous multi-shelled structure can not only make the active materials easier to be infiltrated in the electrolyte, but also provide convenient access to Li ion ingress/egress and have more locations (such as hollow interior and defects in the multi-shells of hollow spheres) for Li ion storage, resulting in shorten path of Li^+ diffusion, high capacity[3] and excellent rate ability. Second, the void space effectively accommodates the dramatic volume change and alleviates the strain during lithiation/delithiation processes. Third, the shells packed by nanorods could ensure efficient electron transport.

4. Conclusions

In summary, unique α-Fe_2O_3 porous multi-shelled hollow spheres (α-Fe_2O_3 PMSHSs) are synthesized by a L-histidine-assisted template-free hydrothermal method followed by annealing in air, in which L-hisitidine has been used as a morphology controlling agent in the synthesis of the α-Fe_2O_3 for the first time. The current micro/nano structure of Fe_2O_3 provides short distance for the migration of Li^+, and accommodates large volume change during charge/discharge process. When served as anode material for lithium ion batteries, the α-Fe_2O_3 PMSHSs exhibit an outstanding electrochemical performance in terms of excellent cycling stability (~869.9 mAh g^{-1} at a current density of 400 mA g^{-1} after 300 cycles) and superior capability (~1202.8 mAh g^{-1} at a current of 100 mA g^{-1} after 128 cycles). Moreover, it presents good rate capability. A reversible charge capacity as high as 498.1 mAh g^{-1} can be measured at a high current density of 6000 mA g^{-1}. The synthesis method is highlighted by its simplicity and promising industrial merits. This template-free route can be extended to the fabrication of other oxides composition with special nanoarchitecture. And the morphology controlling mechanism of L-histidine deserves a further study.

Notes and references

[a] *School of Chemical Engineering, Sichuan University, Chengdu 610065, P. R. China. Fax: +86-28-85406702; Tel: +86-28-85406702; E-mail: xiaodong2009@163.com*

[b] *College of Energy, State Key Laboratory of Physical Chemistry of Solid Surfaces, College of Chemistry and Chemical Engineering, Xiamen University, Xiamen 361005, P. R. China. Fax: +86-592-2180181; Tel: +86-592-2180181; E-mail: jtli@xmu.edu.cn*

† Electronic Supplementary Information (ESI) available: See DOI: 10.1039/b000000x/ for more detailed experiment procedures.

Acknowledgements

This work was financially supported by NSFC (Grant no.21373008, 21321062 and 21273184).

1. X. W. Lou, L. A. Archer and Z. Yang, *Advanced Materials*, 2008, **20**, 3987-4019.
2. J. Liu, F. Liu, K. Gao, J. Wu and D. Xue, *Journal of Materials Chemistry*, 2009, **19**, 6073-6084.
3. J. Liu, H. Xia, D. Xue and L. Lu, *Journal of the American Chemical Society*, 2009, **131**, 12086–12087.
4. M. Yang, J. Ma, C. Zhang, Z. Yang and Y. Lu, *Angewandte Chemie International Edition*, 2005, **44**, 6727-6730.
5. X. W. Lou, C. Yuan and L. A. Archer, *Small*, 2007, **3**, 261-265.
6. Z. Dong, X. Lai, J. E. Halpert, N. Yang, L. Yi, J. Zhai, D. Wang, Z. Tang and L. Jiang, *Advanced Materials*, 2012, **24**, 1046-1049.
7. X. Lai, J. Li, B. A. Korgel, Z. Dong, Z. Li, F. Su, J. Du and D. Wang, *Angewandte Chemie*, 2011, **123**, 2790-2793.
8. X. Wang, X. L. Wu, Y. G. Guo, Y. Zhong, X. Cao, Y. Ma and J. Yao, *Advanced Functional Materials*, 2010, **20**, 1680-1686.
9. H. Xu and W. Wang, *Angewandte Chemie International Edition*, 2007, **46**, 1489-1492.
10. P. Poizot, S. Laruelle, S. Grugeon, L. Dupont and J. M. Tarascon, *Nature*, 2000, **407**, 496-499.
11. J. Maier, *Nat Mater*, 2005, **4**, 805-815.
12. M. V. Reddy, G. V. Subba Rao and B. V. R. Chowdari, *Chemical reviews*, 2013, **113**, 5364-5457.
13. X. Li, L. Qiao, D. Li, X. Wang, W. Xie and D. He, *Journal of Materials Chemistry A*, 2013, **1**, 6400-6406.
14. D. Larcher, D. Bonnin, R. Cortes, I. Rivals, L. Personnaz and J.-M. Tarascon, *Journal of The Electrochemical Society*, 2003, **150**, A1643-A1650.
15. F. Jiao, J. Bao and P. G. Bruce, *Electrochemical and Solid-State Letters*, 2007, **10**, A264-A266.
16. M. V. Reddy, T. Yu, C. H. Sow, Z. X. Shen, C. T. Lim, G. V. Subba Rao and B. V. R. Chowdari, *Advanced Functional Materials*, 2007, **17**, 2792-2799.
17. C. Wu, P. Yin, X. Zhu, C. OuYang and Y. Xie, *The journal of physical chemistry. B*, 2006, **110**, 17806-17812.
18. K. Li, H. Xie, J. Liu, Z. Ma, Y. Zhou and D. Xue, *Physical Chemistry Chemical Physics*, 2013, **15**, 17658.
19. Z. Li, X. Wang, C. Wang and L. Yin, *RSC Advances*, 2013, **3**, 17097-17104.
20. J. Liu, J. Jiang, D. Qian, G. Tan, S. Peng, H. Yuan, D. Luo, Q. Wang and Y. Liu, *RSC Advances*, 2013, **3**, 15457-15466.
21. H.-S. Lim, Y.-K. Sun and K.-D. Suh, *Journal of Materials Chemistry A*, 2013, **1**, 10107-10111.
22. F. Cheng, K. Huang, S. Liu, J. Liu and R. Deng, *Electrochimica Acta*, 2011, **56**, 5593-5598.
23. F. Han, D. Li, W.-C. Li, C. Lei, Q. Sun and A.-H. Lu, *Advanced Functional Materials*, 2013, **23**, 1692-1700.
24. Y. Li, C. Zhu, T. Lu, Z. Guo, D. Zhang, J. Ma and S. Zhu, *Carbon*, 2013, **52**, 565-573.
25. H. Liu, D. Wexler and G. Wang, *Journal of Alloys and Compounds*, 2009, **487**, L24-L27.
26. J. Chen, L. Xu, W. Li and X. Gou, *Advanced Materials*, 2005, **17**, 582-586.
27. J. Zhu, Z. Yin, D. Yang, T. Sun, H. Yu, H. E. Hoster, H. H. Hng, H. Zhang and Q. Yan, *Energy & Environmental Science*, 2013, **6**, 987-993.
28. H. Xiao, Y. Xia, W. Zhang, H. Huang, Y. Gan and X. Tao, *Journal of Materials Chemistry A*, 2013, **1**, 2307-2312.
29. L. Zhang, H. B. Wu, S. Madhavi, H. H. Hng and X. W. Lou, *Journal of the American Chemical Society*, 2012, **134**, 17388-17391.
30. C. Shi, T. Cao, C. Cao, D. Wu, Y. Li, M. Wang and W. Mo, *Materials Letters*, 2012, **83**, 35-38.
31. Z. Liu and S. W. Tay, *Materials Letters*, 2012, **72**, 74-77.
32. C. Wang, L. Wang and K. Tang, *International Journal of Electrochemical Science*, 2013, **8**.
33. L. Yu, Y. Caiyun, D. Wei, G. Xuehui, Q. Haisheng, H. Yong and H. Xiao, *Journal of Alloys and Compounds*, 2013, **551**.
34. L. Zhou, H. Xu, H. Zhang, J. Yang, S. B. Hartono, K. Qian, J. Zou and C. Yu, *Chemical communications*, 2013, **49**, 8695-8697.
35. M. Y. Son, Y. J. Hong, J.-K. Lee and Y. Chan Kang, *Nanoscale*, 2013, **5**, 11592-11597.
36. K. Chen, Y. Dong Noh, K. Li, S. Komarneni and D. Xue, *The Journal of Physical Chemistry C*, 2013, **117**, 10770–10779.
37. J. Zhang, Y. Sun, Y. Yao, T. Huang and A. Yu, *Journal of Power Sources*, 2013, **222**, 59-65.
38. Z. Du, S. Zhang, J. Zhao, X. Wu and R. Lin, *Journal of Nanoscience and Nanotechnology*, 2013, **13**, 3602-3605.
39. D. Du and M. Cao, *J Phys Chem C Nanomater Interfaces*, 2008, **112**, 10754-10758.

40. H. Cao, R. Liang, D. Qian, J. Shao and M. Qu, *The Journal of Physical Chemistry C*, 2011, **115**, 24688–24695.
41. H. A. Petrosyan, H. A. Karapetyan and A. M. Petrosyan, *Journal of Molecular Structure*, 2006, **794**, 160–167.
42. H. Qian, G. Lin, Y. Zhang, P. Gunawan and R. Xu, *Nanotechnology*, 2007, **18**, 355602.
43. H. Cao, H. Zheng, K. Liu and R. Fu, *Crystal Growth & Design*, 2010, **10**, 597–601.
44. N. Yan, X. Zhou, Y. Li, F. Wang, H. Zhong, H. Wang and Q. Chen, *Scientific reports*, 2013, **3**, 3392.
45. H. Liu, G. Wang, J. Park, J. Wang, H. Liu and C. Zhang, *Electrochimica Acta*, 2009, **54**, 1733-1736.
46. S. Laruelle, S. Grugeon, P. Poizot, M. Dollé, L. Dupont and J.-M. Tarascon, *Journal of The Electrochemical Society*, 2002, **149**, A627-A634.
47. Y. Han, Y. Wang, L. Li, Y. Wang, L. Jiao, H. Yuan and S. Liu, *Electrochimica Acta*, 2011, **56**, 3175-3181.
48. J.-T. Li, V. Maurice, J. Swiatowska-Mrowiecka, A. Seyeux, S. Zanna, L. Klein, S.-G. Sun and P. Marcus, *Electrochimica Acta*, 2009, **54**, 3700-3707.
49. J. Zhang, T. Huang, Z. Liu and A. Yu, *Electrochemistry Communications*, 2013, **29**, 17-20.
50. G.-L. Xu, Y.-F. Xu, H. Sun, F. Fu, X.-M. Zheng, L. Huang, J.-T. Li, S.-H. Yang and S.-G. Sun, *Chemical communications*, 2012, **48**, 8502-8504.
51. J. J. Zhang, Y. L. Chen, Y. F. Sun, T. Huang and A. S. Yu, *Rsc Advances*, 2013, **3**, 20639-20646.
52. Y.-M. Lin, P. R. Abel, A. Heller and C. B. Mullins, *The Journal of Physical Chemistry Letters*, 2011, **2**, 2885-2891.
53. S.-L. Chou, J.-Z. Wang, D. Wexler, K. Konstantinov, C. Zhong, H.-K. Liu and S.-X. Dou, *Journal of Materials Chemistry*, 2010, **20**, 2092-2098.
54. B. Wang, J. S. Chen, H. B. Wu, Z. Wang and X. W. Lou, *Journal of the American Chemical Society*, 2011, **133**, 17146-17148.
55. W.-J. Yu, P.-X. Hou, L.-L. Zhang, F. Li, C. Liu and H.-M. Cheng, *Chemical communications*, 2010, **46**, 8576-8578.
56. X. Zhu, Y. Zhu, S. Murali, M. D. Stoller and R. S. Ruoff, *ACS Nano*, 2011, **5**, 3333-3338.
57. G. Wang, H. Wang, S. Cai, J. Bai, Z. Ren and J. Bai, *Journal of Power Sources*, 2013, **239**, 37-44.
58. H.-D. Oh, S.-W. Lee, S.-O. Kim and J. K. Lee, *Journal of Power Sources*, 2013, **244**, 575-580.